

RESEARCH ARTICLE

Pressure and ion composition boundaries at Mars

10.1002/2016JA022644

Key Points:

- The pressure and composition boundaries are very similar
- Not only the plasma sheet but also the full volume of the lobes are dominated by planetary ions
- The boundary layers are about 1–1.5 R_M thick in the near-tail region, and this thickness increases with distance down the tail

Correspondence to:

S. Xu,
shaosui.xu@ssl.berkeley.edu

Citation:

Xu, S., M. W. Liemohn, C. Dong, D. L. Mitchell, S. W. Bougher, and Y. Ma (2016), Pressure and ion composition boundaries at Mars, *J. Geophys. Res. Space Physics*, 121, 6417–6429, doi:10.1002/2016JA022644.

Received 29 FEB 2016

Accepted 20 JUN 2016

Accepted article online 27 JUN 2016

Published online 15 JUL 2016

Shaosui Xu^{1,2}, Michael W. Liemohn², Chuanfei Dong^{2,3}, David L. Mitchell¹, Stephen W. Bougher², and Yingjuan Ma⁴

¹Space Science Laboratory, University of California, Berkeley, California, USA, ²Department of Climate and Space Sciences and Engineering, University of Michigan, Ann Arbor, Michigan, USA, ³Princeton Plasma Physics Laboratory, Princeton University, Princeton, New Jersey, USA, ⁴Institute of Geophysics and Planetary Physics, University of California, Los Angeles, California, USA

Abstract This study analyzes results from a multifluid MHD simulation to investigate the shape and structure of the pressure and composition boundaries at Mars, which can provide physical insight for the observational analysis. These boundaries are examined via the unity contours and gradients of the plasma β , as well as β^* , which includes the dynamic pressure in the numerator, and the ion mass and number density ratios. It is found that unity contours are well aligned with the gradient extrema, indicating that the unity contour is a topological boundary. In addition, these two transitions of pressure and composition are of a thickness of 0.05–0.1 R_M near the subsolar region to 1–1.5 R_M in the tail. The comparison of the pressure and composition boundaries indicates that the two are very similar and that not only the plasma sheet but also the full volume of the lobes are dominated by planetary ions. It suggests that the tail escape for ions not only concentrates in the central plasma sheet but also the magnetic lobes. It is also worthy pointing out that the ion number density ratio unity contour is found to be systematically smaller than other unity boundaries, which calls for attention when the ion number density is used to identify such boundaries. Finally, the comparison between the boundaries of this study and two analytical fittings is carried out. We found a good agreement with the Vignes fitting, with little flaring in the tail, in contrast to a larger flaring angle from the Trotignon fitting.

1. Introduction

Moore and Delcourt [1995] came up with the concept of the geopause, which marks the boundary between solar and terrestrial dominance of near-Earth space. Multiple geopause boundaries exist, depending on the parameter used to define the boundary. The magnetopause is arguably the most well known of these geopause boundaries, but Moore and Delcourt [1995] also discussed the existence of plasma pressure and density geopauses. At such interfaces, energy and particle interchange between the solar wind and the planetary ionospheric plasmas could occur, resulting in dynamics and perturbations that are essential for geostorm development. Such a concept can be applied to other planets, such as Mars, to provide insight into the physics of magnetic topology and ion escape, as one way for cold planetary ions to attain escape energy is through such a coupling with the solar wind plasma at this interface.

Mars is usually classified as an unmagnetized planet in terms of the interaction with solar wind due to the absence of a significant global intrinsic magnetic field. This interaction results in several distinct regions, such as the magnetosheath, the magnetic pileup region, and the tail region [e.g., Nagy *et al.*, 2004; Bertucci *et al.*, 2012]. The existence of localized crustal fields [e.g., Acuna *et al.*, 1999] complicates this interaction [e.g., Brain *et al.*, 2003, 2007; Harnett and Winglee, 2005; Liemohn *et al.*, 2006, 2007; Ma *et al.*, 2014; Dong *et al.*, 2015a; Xu *et al.*, 2014]. The transition between the magnetosheath and the magnetic pileup region has several observational characteristics, which have been identified by different instruments on various spacecraft. One feature is a sharp increase in magnetic field strength coincident with a decrease in field fluctuations, which was observed by Phobos-2 [e.g., Riedler *et al.*, 1989], the Mars Global Surveyor (MGS) spacecraft [e.g., Vignes *et al.*, 2000; Crider *et al.*, 2002; Bertucci *et al.*, 2005], and also the Mars Atmosphere and Volatile Evolution (MAVEN) spacecraft [e.g., Jakosky *et al.*, 2015a, 2015b; Connerney *et al.*, 2015; Halekas *et al.*, 2015; Matsunaga *et al.*, 2015]. These observations resulted in the names known as the magnetic pileup boundary (MPB) or the induced magnetosphere boundary. Another feature of this transition is a switch from solar wind ions to planetary

heavy ions, which was observed by Phobos-2 [e.g., *Sauer et al.*, 1992; *Trotignon et al.*, 1996], Mars Express [e.g., *Dubinin et al.*, 2006, 2008; *Fränz et al.*, 2006], and MAVEN [e.g., *Ma et al.*, 2015; *Dong et al.*, 2015b; *Matsunaga et al.*, 2015]. This resulted in the names including the protonopause and the ion composition boundary (ICB). These boundaries located at the inner side of the magnetosheath were also identified and studied by plenty of simulation efforts [e.g., *Sauer et al.*, 1994; *Ma et al.*, 2002, 2004; *Böβwetter et al.*, 2004; *Brecht*, 1990, 1997; *Harnett and Winglee*, 2005; *Modolo et al.*, 2006; *Kallio et al.*, 2006; *Simon et al.*, 2007; *Brain et al.*, 2010]. In particular, *Fang et al.* [2015] showed the irregularity of MPB and how it varies with the crustal field rotation.

The transition between the magnetosheath and magnetic pileup region at Mars generally resembles Earth's geopause, because of the sharp transitions between the solar wind and planetary plasmas. In this study, we analyze the results from a Block-Adaptive Tree Solar wind Roe-type Upwind Scheme (BATS-R-US) Mars Multifluid MHD model to quantitatively study these boundaries by looking at plasma-type (thermal and dynamic) and magnetic pressures. There are different ways to define such boundaries, such as locations where the dominant contribution to the total pressure changes or where the dominant ion species changes, or where sharp gradients in the pressure terms or composition occur. Pressure and composition boundaries often appear sharp on time series figures of spacecraft observations, particularly on the dayside. Similarly, boundaries identified in simulations are often displayed as lines and surfaces. However, the thicknesses of these transitions are typically not considered, especially downstream of the terminator. Transition thicknesses can be determined both observationally and from simulations, which is useful for assessing the transition from solar wind to planetary influence. In addition, due to limitation of instruments of many spacecraft, the relation of MPB and ICB was not well understood. This study will also present a systematic comparison between the two from a theoretical view.

2. BATS-R-US Mars Multifluid MHD Model Description

The University of Michigan 3-D Block-Adaptive Tree Solar wind Roe-type Upwind Scheme (BATS-R-US) multifluid MHD (MF-MHD) model was initially developed for the Earth environment [*Powell et al.*, 1999; *Glocer et al.*, 2009; *Tóth et al.*, 2012] and then adapted to Mars [*Najib et al.*, 2011; *Dong et al.*, 2014]. The Mars MF-MHD model computes a full set of continuity, momentum, and energy equations for four ion species, H^+ , O^+ , O_2^+ , and CO_2^+ . Due to a much weaker magnetic environment at Mars, and thus a much slower Alfvén speed, the inner boundary of the Mars MF-MHD model is set at 100 km altitude. This altitude is below the ionospheric density peak, thus the model is able to simulate the entire plasma environment around the planet.

The model includes detailed ionospheric chemistry, photoionization, charge exchange, recombination, and electron impact ionization. The chemical reaction schemes are described in *Ma et al.* [2004] and *Najib et al.* [2011]. Electron impact ionization rates are given by *Cravens et al.* [1987], and collision frequencies between species are given by *Schunk and Nagy* [2009]. At the inner boundary, O^+ , O_2^+ , and CO_2^+ are assumed to be in photochemical equilibrium and H^+ is set to be approximately 30% of the solar wind density, to account for proton penetration into the ionosphere. Additionally, the velocity \mathbf{u} is set to be a reflective boundary condition. Furthermore, the ion and electron temperature is set to be the same as the neutral temperature at the inner boundary, given frequent collisions between neutral particles and plasma. The 60° harmonic expansion developed by *Arkani-Hamed* [2001] is incorporated into the MF-MHD model to take into account the crustal fields.

The simulation domain is within $-24R_M \leq X \leq 8R_M$; $-16R_M \leq Y, Z \leq 16R_M$, in a nonuniform spherical grid structure with a radial resolution varying from 5 km near the inner boundary to 1000 km near the outer boundary with an angular resolution of 1.5°–3.0°. R_M is the Mars radius, and the results of this study are shown in the Mars-centered Solar Orbital (MSO) coordinates, with x axis pointing at the Sun, y axis opposite to the Mars orbital direction, and z axis perpendicular to the Mars orbital plane. The neutral atmosphere is adopted from the Mars Global Ionosphere Thermosphere Model [*Bougher et al.*, 2015] for the cold neutral component and from the Mars exosphere Monte Carlo model Adaptive Mesh Particle Simulator (M-AMPS) [*Lee et al.*, 2014a, 2014b, 2015] for the hot neutral corona.

For this study, we have chosen the solar maximum ($F_{10.7} = 200$ solar flux unit, sfu), ($1\text{sfu} = 10^{-22} \text{ W m}^{-2}\text{Hz}^{-1}$) perihelion conditions with the subsolar longitude set to 180°W (strong crustal field regions on the dayside) to explore the boundaries. The solar wind inputs are specified as follows: a density of 4 cm^{-3} , a plasma

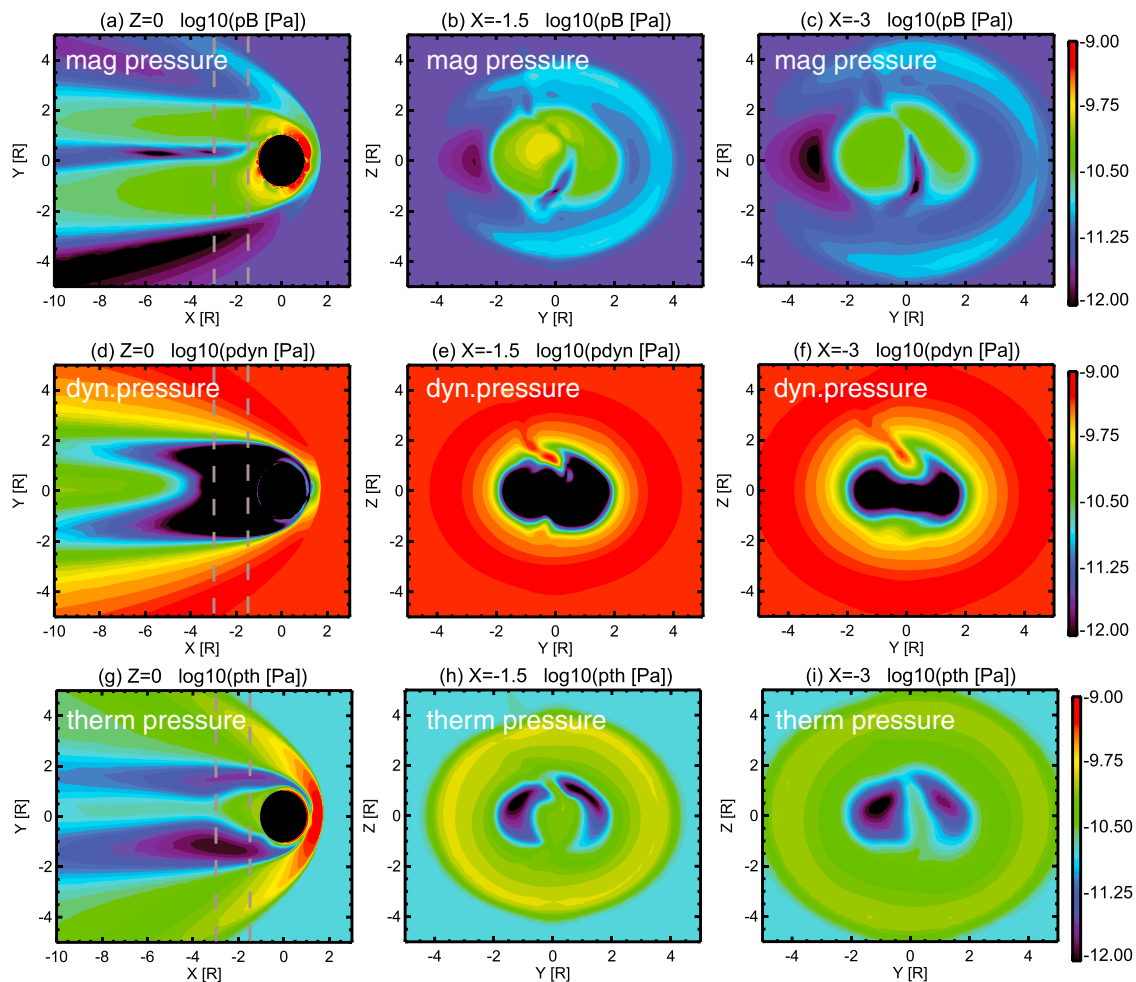


Figure 1. (a–c) the magnetic pressure (Pa), (d–f) the dynamic pressure (Pa), and (g–i) the thermal pressure (Pa). (a, d, g) $Z = 0$, (b, e, h) $X = -1.5R_M$, and (c, f, i) $X = -3R_M$ in MSO coordinates. The values are logarithmic scale. The two vertical dashed lines in the first column mark the positions of the two X slices in the second and third columns.

temperature of 3.5×10^5 K, a velocity of 400 km/s, and the interplanetary magnetic field (IMF) being 3 nT in a typical away sector (IMF pointing away from the Sun) Parker spiral pattern with an angle of 56° . These inputs correspond to Case 17 of *Dong et al. [2015a]*.

3. Pressure Boundary

In the Mars plasma environment, the total pressure consists of three terms: magnetic pressure, dynamic pressure, and thermal pressure. These three pressures from the MF-MHD run are shown in the three rows, respectively, in Figure 1 and the three columns planar cuts $Z = 0$, $X = -1.5R_M$, and $X = -3R_M$ in MSO coordinates. Typical structures of the interaction between an unmagnetized planet and the solar wind can be identified in the $Z = 0$ plane. The bow shock is located $\sim 1.7 R_M$ at the subsolar point, upstream of which the solar wind dynamic pressure dominates. After the bow shock, most (not all) of the dynamic pressure is converted into thermal and magnetic pressure, with thermal pressure prevailing near the subsolar region, and dynamic pressure progressively more important in the flanks. Closer to the planet, magnetic pressure accounts for a larger fraction of the total pressure because of mass loading effects and localized crustal fields. For $X < 0$, the dynamic pressure dominates the magnetosheath once behind the obstacle. In the central plasma sheet, the thermal pressure dominates the near Mars region ($-5 < X < 0$) and the dynamic pressure prevails in the distant tail ($X < -5$). Complementing the plasma pressure at $X < 0$, high magnetic pressures highlight two magnetic lobes, separated by the central plasma sheet. The magnetic pressure differs

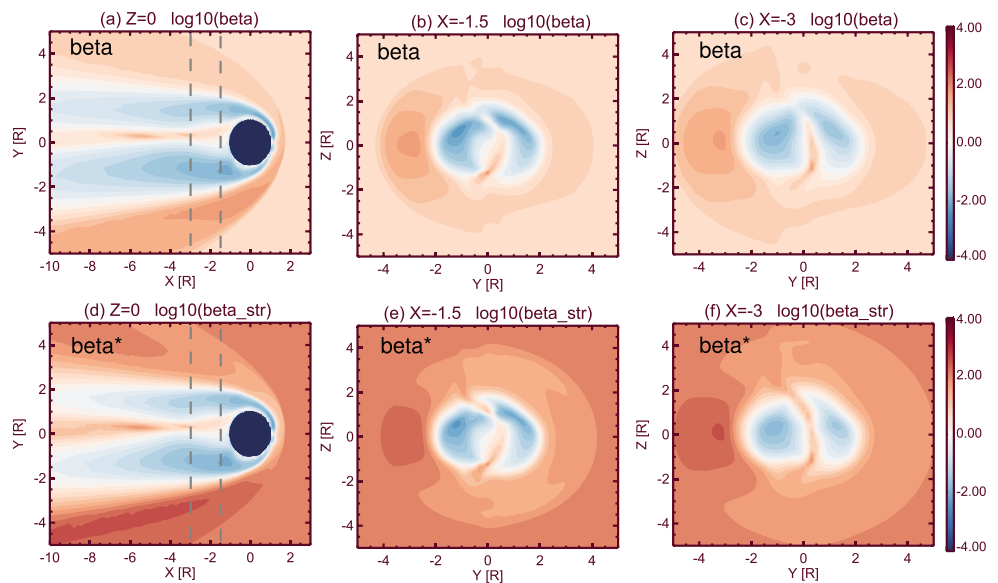


Figure 2. Plasma beta (β), i.e., the ratio of the plasma thermal pressure and the magnetic pressure, is shown at (a) $Z = 0$, (b) $X = -1.5R_M$, and (c) $X = -3R_M$, while β^* , which is the sum of the plasma thermal pressure and dynamic pressure divided by the magnetic pressure, is shown in at (d) $Z = 0$, (e) $X = -1.5R_M$, and (f) $X = -3R_M$. The values are logarithmic scale. The two vertical dashed lines in Figures 2a and 2d mark the positions of the two X slices in Figures 2b and 2e and Figures 2c and 2f.

significantly when comparing the parallel and perpendicular regions (IMF parallel and perpendicular to the shock normal, respectively) of the shock as shown in Figures 1a–1c: on the more perpendicular side of the shock (+ Y), there is a prominent increase in magnetic pressure, which is not present on the more parallel side of the shock ($-Y$). Pressures are also shown in the two selected cuts down tail, $X = -1.5R_M$ and $X = -3.0R_M$, where two magnetic lobe structures can be easily identified.

To help distinguish the different pressure regimes, we calculate the plasma beta ($\beta = p_{th}/p_B$), i.e., the ratio of the plasma thermal pressure (p_{th}) and the magnetic pressure (p_B), which is shown in Figures 2a–2c, at $Z = 0$, $X = -1.5R_M$, and $X = -3R_M$, respectively. However, the plasma dynamic pressure increases downstream of the planet, as seen in Figures 1d–1f. Hence, we define $\beta^* = (p_{th} + p_{dyn})/p_B$, which is the sum of the plasma thermal pressure (p_{th}) and dynamic pressure (p_{dyn}) divided by the magnetic pressure (p_B). In other words, if $\beta^* > 1$, the region is dominated by the plasma-type pressures, or vice versa. Figures 2d–2f illustrate the distribution of β^* at the three cuts. The blue color highlights regions dominated by the magnetic pressures, while the red shading reveals areas dominated by the plasma-type pressures, with the white showing parity. Overall, β and β^* depict a similar pattern, with the magnetic pressure dominating the two lobes and near the planet on the dayside, and plasma-type pressures prevail in the plasma sheet, magnetosheath, and beyond. The main difference is that β^* defines a smaller magnetic dominant region, as the numerator includes two pressure terms. To show this more clearly, Figures 3a and 3b illustrate the contours of $\beta = 1$ and $\beta^* = 1$, respectively. The view in both panels of Figure 3 is from above the ecliptic plane in the afternoon sector. The green translucent surface shows the unity contour. For reference of scale, the inner, almost spherical surface is in the ionosphere near the inner boundary of the simulation domain. Both unity contours enclose the tail lobes, but the β unity contour has a larger extent and extends more than $10R_M$ downstream of the planet.

Another way to identify pressure boundaries is to compute the gradients of β and β^* . Figure 4 shows the gradient of the logarithm of β (a–c) and β^* (d–f). The gradient is calculated along the radial direction in each plane. For the two X cuts, it is appropriate to assume small gradients along the X direction. For the $Z = 0$ plane, however, such a radial gradient ($r = \sqrt{X^2 + Y^2}$) is less suitable far down the tail because the gradient should be primarily in the cylindrical radial direction, i.e., in the $|Y|$ direction for this plane. Hence, we should focus more on the dayside for the gradients on the $Z = 0$ plane. Also, note that the color bars are in different ranges for

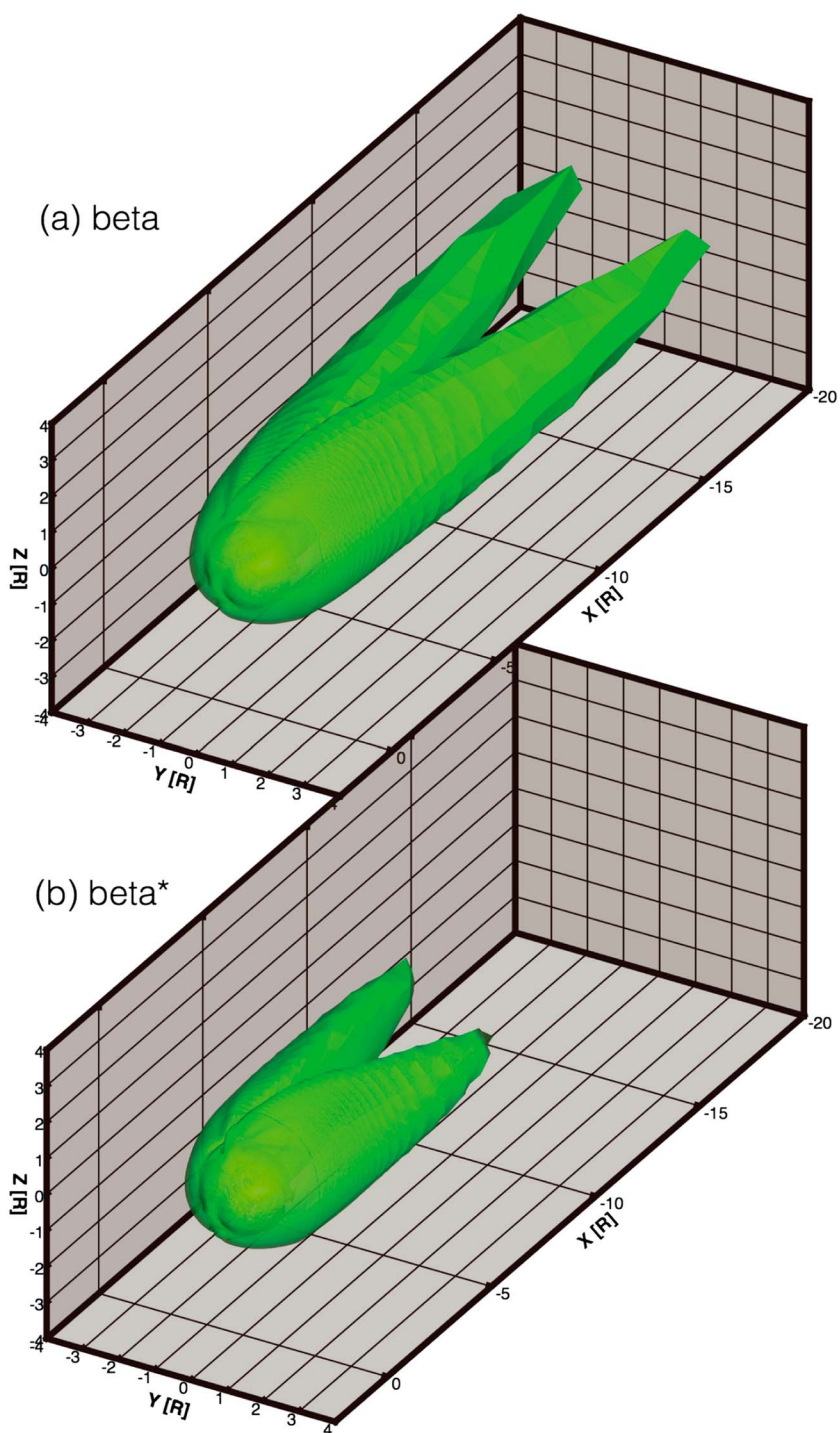


Figure 3. The contours of (a) $\beta = 1$ and (b) $\beta^* = 1$.

three planes. As we can see, the strong gradient layers for betas are thin on the dayside, becoming increasingly thicker and more subdued with distance downstream of the planet. The thickness of the boundary layer in the tail is of $1 - 1.5 R_M$. In addition, the unity boundaries of both β and β^* (black crosses) are coincident with the strong gradient layers (the dark red region where the value is greater than 1, indicating an order of magnitude change per Mars radius). On the other hand, even though the unity contour extends to large distances down the tail ($> 10 R_M$), the transition becomes too gradual, as indicated by the large area colored white in Figures 2a

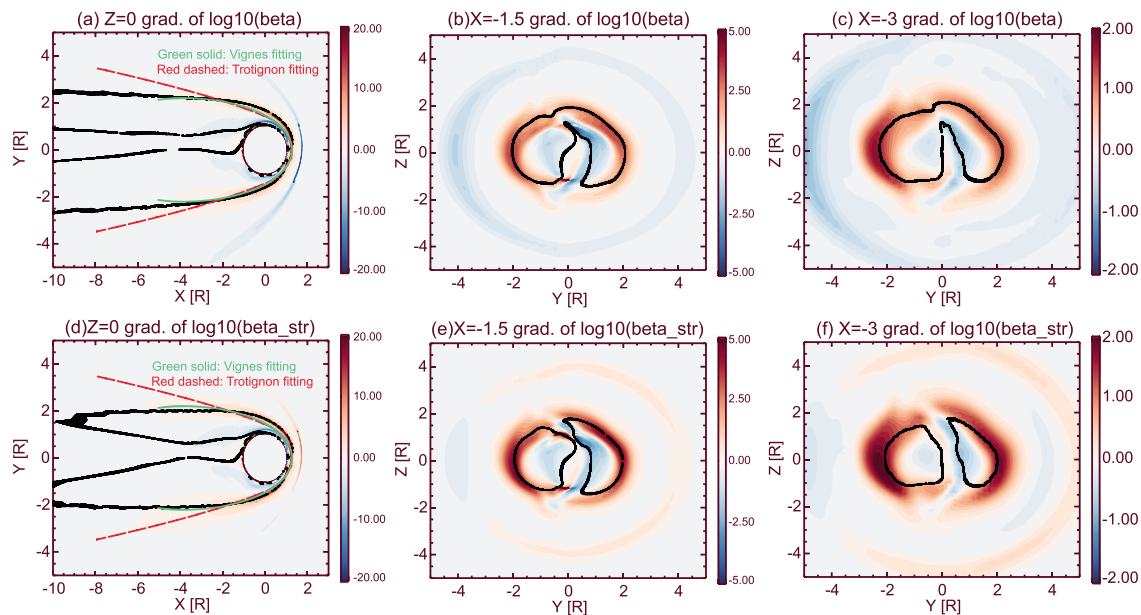


Figure 4. The gradient of the logarithm of (a–c) β and (d–f) β^* . The columns are for $Z = 0$ (Figures 4a and 4d), $X = -1.5R_M$ (Figures 4b and 4e), and $X = -3R_M$ (Figures 4c and 4f) in MSO coordinates. The black crosses highlight the unities of β and β^* , as extracted from Figure 2. The green solid line and red dashed line in Figures 4a and 4d represent the MPB fitting from Vignes et al. [2000] and Trotignon et al. [1996], respectively.

and 2d for $X < -4R_M$, to be a meaningful boundary indicator. In addition, the grid resolution is rather coarse in the far tail. Hence, we only select y - z planar cuts as far as $3R_M$ down tail.

4. Ion Composition Boundary

As mentioned above, four ion species, H^+ , O^+ , O_2^+ , and CO_2^+ , are included in the simulation. Figure 5 shows the H^+ mass (also number) density, the heavy ion (CO_2^+ , O^+ , and O_2^+) mass density, and the heavy ion number density from the MF-MHD model in the three rows, respectively. The three columns again are for $Z = 0$, $X = -1.5R_M$, and $X = -3R_M$ cuts. H^+ dominates the sheath and beyond (Figures 5a–5c), and high H^+ density is also seen near the planet (Figures 5a and 5b) of a planetary origin as the density is too high to be solar wind originated. High heavy ion density is seen near the planet as well as the central plasma sheet, as expected. Further down the tail, the heavy ion escape is more concentrated in the plasma central sheet, as seen by comparing Figures 5e and 5h with Figures 5f and 5i. The energetic loss plume due to pick up ions by the convective electric field carried by the solar wind ($\mathbf{E} = -\mathbf{U} \times \mathbf{B}$) is also seen in Figures 5e, 5f, 5h, and 5i, oriented in the $+Z$ direction due to the $+By$ component of the input IMF, but less prominent in the number density figures.

To define a model-based ion composition boundary, we calculate the ratio of the H^+ density and the heavy ion density, for both mass density and number density. The results for the aforementioned three cuts are shown in Figure 6, the first row for the mass density ratio and the second row for the number density ratio. An interesting finding is that the white color, indicating a ratio of 1, encloses both the plasma sheet and the magnetic lobes, indicating that both regions are dominated by planetary heavy ions. Again, for $X < -4R_M$, the transition from H^+ to heavy ions becomes less distinct with increasing distance down the tail.

Figure 7 shows the unity contours for the mass density ratio (a) and the number density ratio (b). The view is from slightly above the ecliptic plane and slightly sunward of the dusk terminator. Both unity boundaries extend very far down the tail ($> 10R_M$) and also overlap with the magnetic lobes. The mass density unity contour is larger than the number density ratio unity contour because it has a mass multiplier. Also, the plume is more prominent and extended for the mass density ratio unity contour but barely seen in the number density ratio unity contour.

In a similar fashion, the gradients of the logarithms of the density ratios are also calculated, shown in Figures 8a–8c for the mass density ratio and Figures 8d–8f for the number density ratio. The gradients are

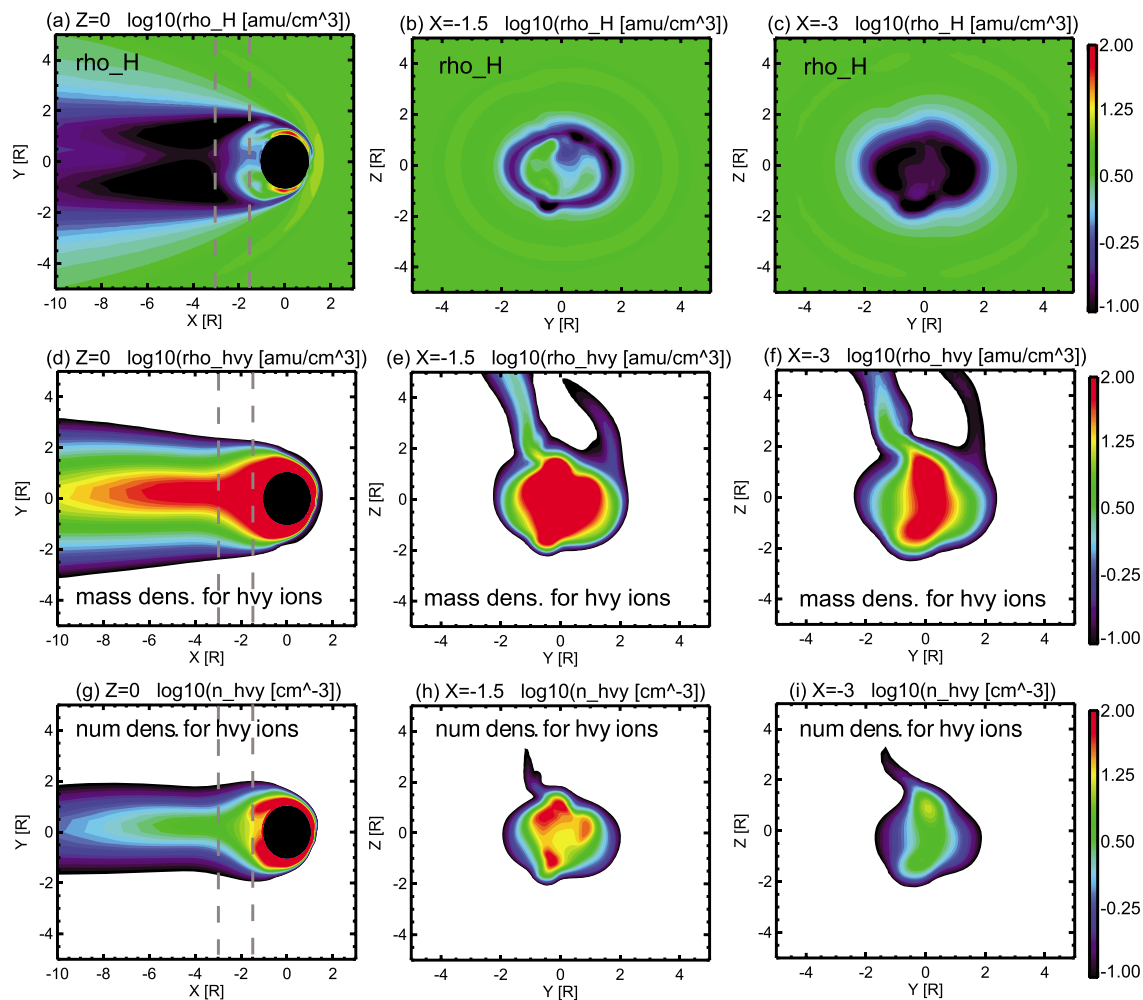


Figure 5. (a–c) The mass density of H^+ (amu/cm^3), (d–f) the mass density (amu/cm^3) of heavy ions (CO_2^+ , O^+ , and O_2^+), and (g–i) the number density (cm^{-3}) of heavy ions. The columns are for (a, d, g) $Z = 0$, (b, e, h) $X = -1.5R_M$, and (c, f, i) $X = -3R_M$ in MSO coordinates. The values are logarithmic scale. The two vertical dashed lines in Figures 5a, 5d, and 5g mark the positions of the two X slices in Figures 5b, 5e, and 5h and Figures 5c, 5f, and 5i.

computed in the same way as the betas. Again, thin and sharp strong gradient layers are seen on the dayside (Figures 8a and 8d) and also coincide with the unity boundaries, marked by the black crosses. In the tail (Figures 8b, 8c, 8e, and 8f), the strong gradient layers, again, are of a thickness of $1 - 1.5 R_M$, similar to Figure 4, and become thicker further down tail, comparing Figure 8b with Figure 8c and Figure 8e with Figure 8f. Furthermore, the gradients are about the same for the mass density ratio and the number density ratio as the mass multiplier is mostly canceled from the logarithmic gradient calculation. With that as a reference, the unity of the mass density ratio, naturally larger, marks the center of the strong gradient layer, while the unity of the number density ratio is more closely aligned with the inner edge.

5. Comparisons

Now that we have defined model-based pressure and composition boundaries, resembling the observationally based magnetic pileup and ion composition boundaries, the next step is to compare these boundaries. Figure 9 shows the comparisons between the pressure boundary and the ion composition boundary via different methods. The three columns are for $Z = 0$ (Figures 9a, 9d, and 9g), $X = -1.5 R_M$ (Figures 9b, 9e, and 9h), and $X = -3 R_M$ (Figures 9c, 9f, and 9i). Figures 9a–9c show the unities of β , β^* , ion mass density ratio, and ion number density ratio, colored in black, blue, green, and red, respectively. For the equatorial plane, we have zoomed in to focus on the dayside. The unity contours for these four quantities are basically on top of each other and exhibit asymmetry about the X axis probably due to the effects of quasi-parallel and quasi-perpendicular

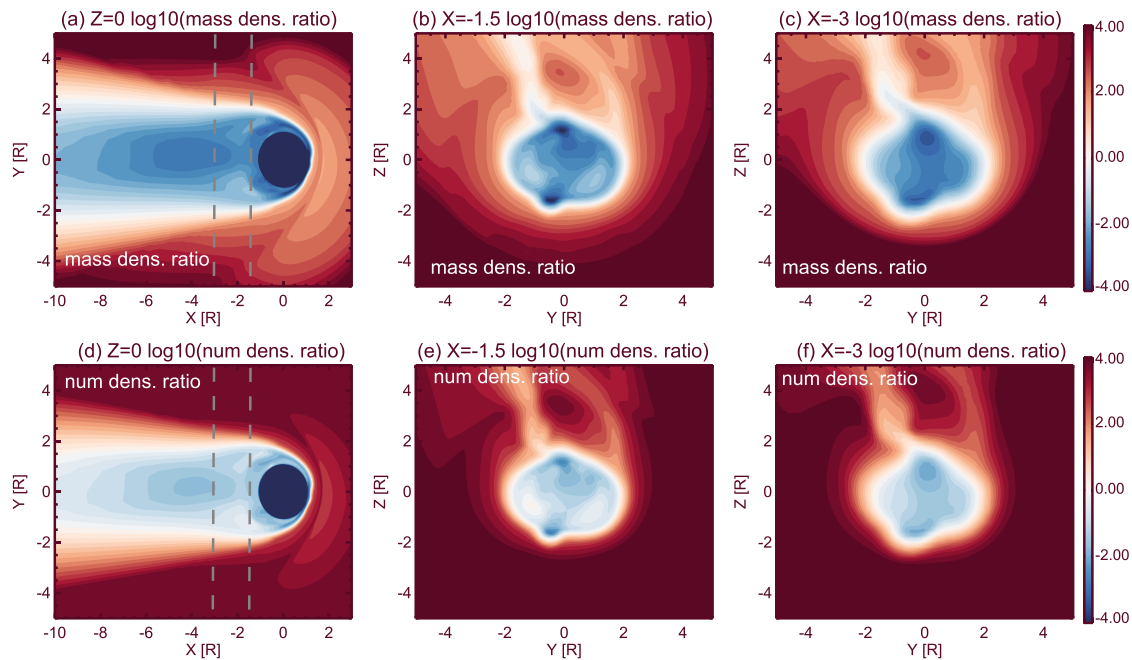


Figure 6. The ratio of the mass density of H^+ and heavy ions is shown at (a) $Z = 0$, (b) $X = -1.5R_M$, and (c) $X = -3R_M$, while the ratio of the number density of H^+ and heavy ions is shown at (d) $Z = 0$, (e) $X = -1.5R_M$, and (f) $X = -3R_M$. The values are logarithmic scale. The two vertical dashed lines in Figures 6a and 6d mark the positions of the two X slices in Figures 6b and 6e and Figures 6c and 6f.

shocks (see Figure 1a). The two betas also have another inner unity curve, a balance between the ionospheric plasma-type pressure and the magnetic pressure. For the tail cuts, the unities of β , β^* , and ion mass density ratio mostly coincide on the outer edge at $X = -1.5R_M$, while the ion number density ratio unity is systematically smaller. Further down tail, at $X = -3R_M$ (Figure 9c), the β unity is the outmost, and then slightly inward are the overlapping β^* and ion mass density ratio unities, and the ion number density ratio unity is located as the innermost curve.

Upstream of the planet ($X > 0$) along the Mars-Sun line (Figure 9d), transitions in the pressure and density ratios are apparent at the bow shock ($X = 1.75$) and near the MPB ($X = 1.2-1.3$). Downstream of the planet ($X < 0$), the unities begin to separate along Y with distance down tail as the transition from plasma-type pressure and H^+ dominance to magnetic pressure and heavy ion dominance becomes more gradual, as shown in Figures 9b, 9e, and 9h and Figures 9c, 9f, and 9i. Each quantity has sharper transitions closer to the planet.

To better compare the locations of unities with the locations of maximum gradient in the various quantities, the bottom row shows the gradient of the logarithmic values along the Mars-Sun line (Figure 9g) and in the cross-tail Y direction at $X = -1.5$ and $X = -3$ (Figures 9h and 9i), with color-coded vertical dashed lines marking the innermost and outermost unity locations. The maximum gradients of the four quantities are nearly colocated. The tailward magnetosheath ($2.5 < |Y| < 4R_M$ and $-3 < |Y| < -1.5R_M$ approximately) is a region dominated by H^+ (density ratio $\gg 1$) and dynamic pressure ($\beta^* \gg \beta$). At the inner edge of this region ($|Y| \sim 2-2.5R_M$), the composition and all of the pressure terms exhibit sharp gradients at nearly the same location (Figures 9b, 9e, and 9h and Figures 9c, 9f, and 9i), suggesting that all mark the same physical transition. Third, gradient extrema agree very well with the unities of β , β^* , and ion mass density ratio, while the ion number density unity is located systematically inward of the gradient extrema (Figures 8 and 9). Thus, the unities in β , β^* , and mass density ratio provide convenient proxies for the boundaries between distinct regions of the Mars plasma environment. This also shows that the same physical boundary may be identified using different measurement techniques.

Along the Mars-Sun line (Figure 9g), a strong gradient layer for all quantities is seen at the bow shock ($X \sim 1.7R_M$) with a thickness of about $0.1R_M$ (300–400 km). Downstream of the bow shock, near $1.25R_M$, a positive gradient layer for β and β^* (nearly identical due to a negligible dynamic pressure) is seen with a thickness of $\sim 0.1R_M$. The behavior of the ion density ratio near $1.25R_M$ is slightly different. Both the mass and number

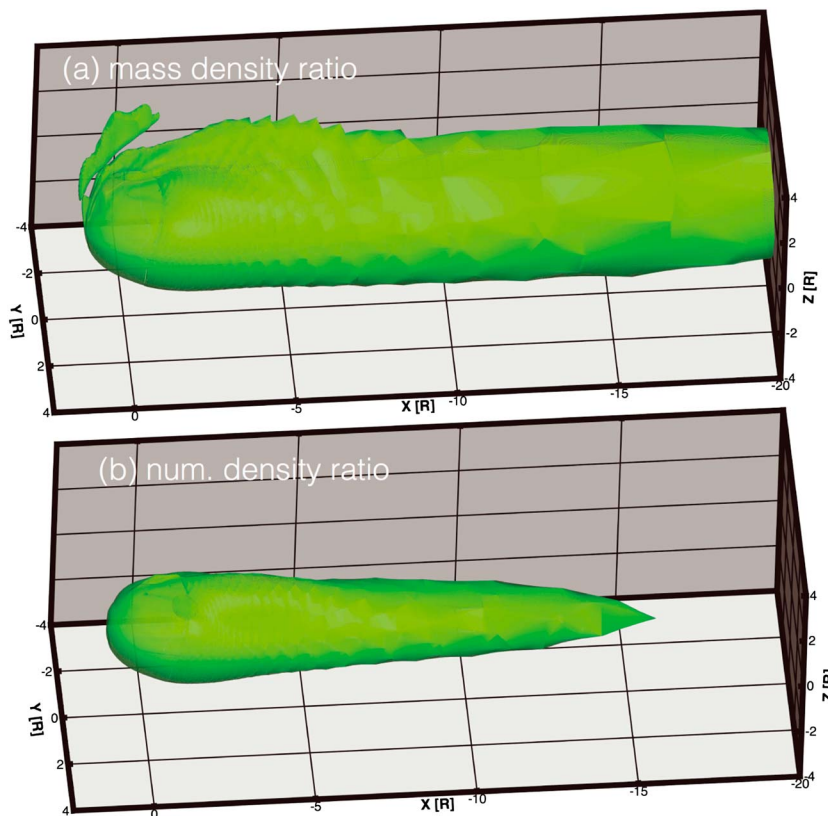


Figure 7. The contours of the (a) ion mass density ratio = 1 and the (b) ion number density ratio = 1.

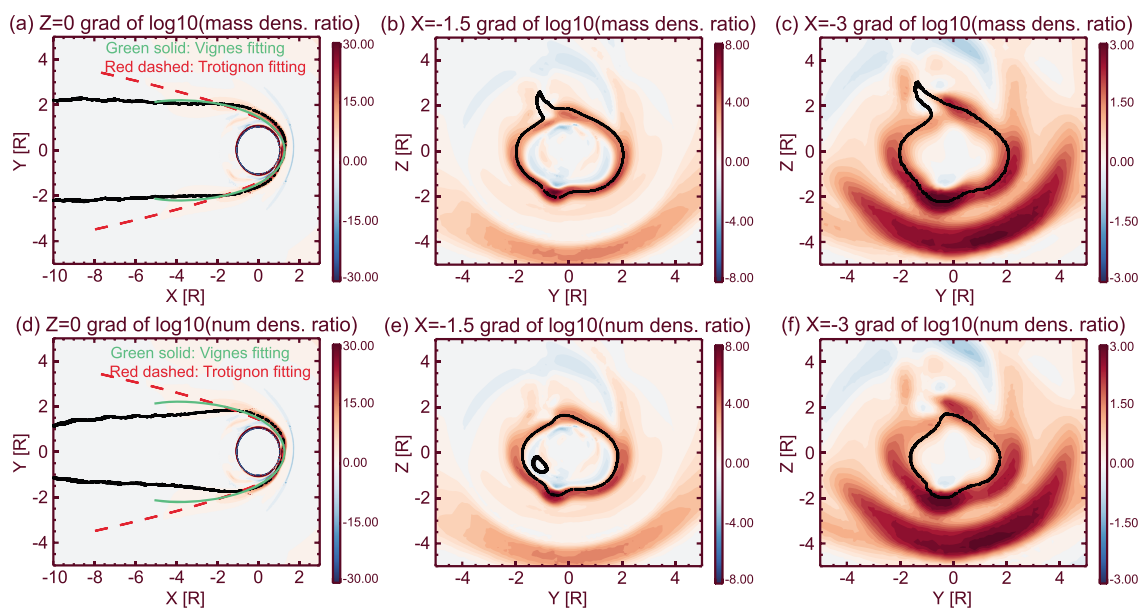


Figure 8. The gradient of the logarithm of the (a–c) ion mass density ratio and the (d–f) ion number density ratio. The three cuts $Z = 0$ (Figures 8a and 8d), $X = -1.5R_M$ (Figures 8b and 8e), and $X = -3R_M$ (Figures 8c and 8f) in MSO coordinates. The black crosses highlight the unities of the ratios, as extracted from Figure 6. The green solid line and red dashed line in Figures 8a and 8d represent the MPB fitting from *Vignes et al.* [2000] and *Trotignon et al.* [2006], respectively.

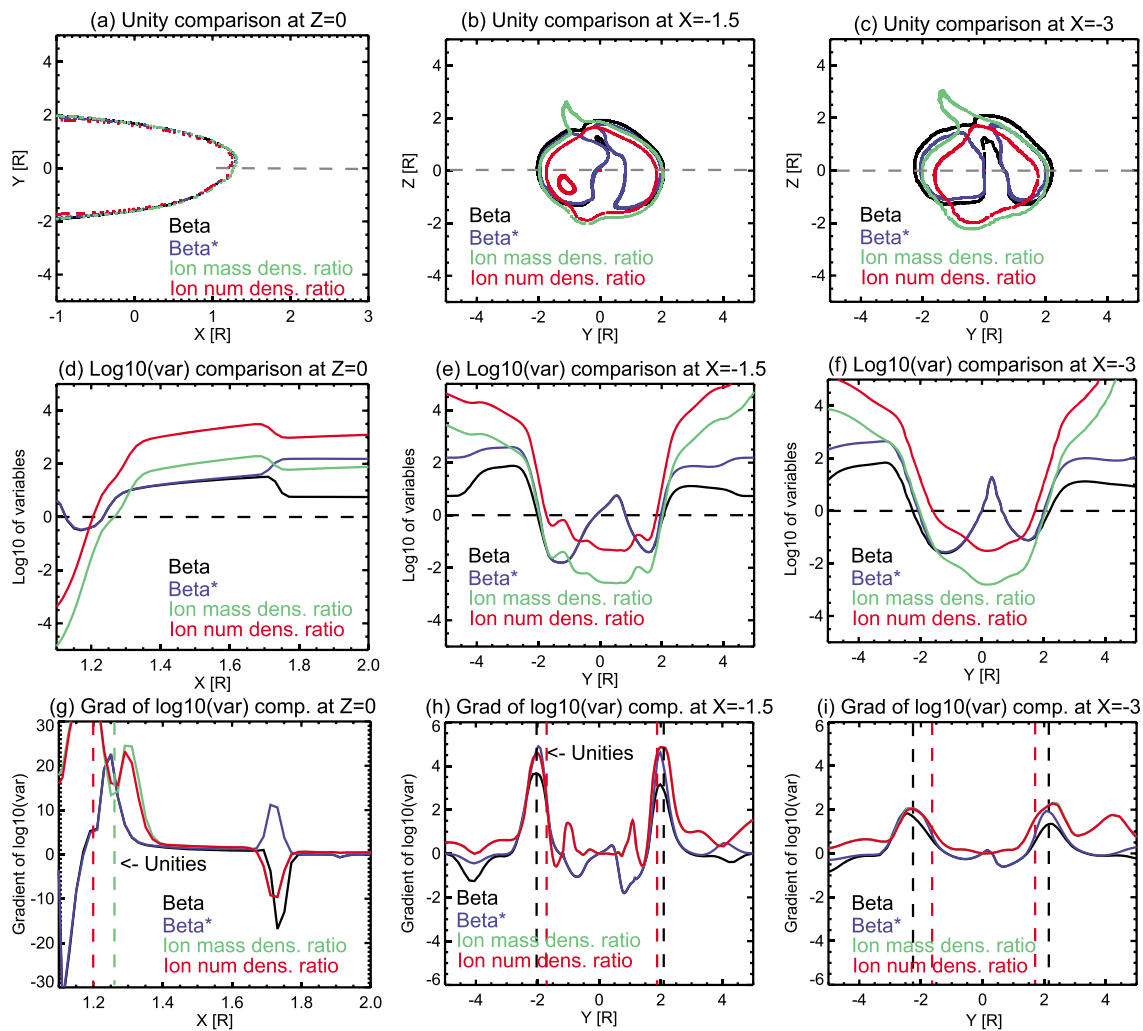


Figure 9. Comparison of unities and gradients at (a, d, g) $Z = 0$, (b, e, h) $X = -1.5R_M$, and (c, f, i) $X = -3R_M$. The unities of β , β^* , ion mass density ratio, and ion number density ratio, colored in black, blue, green, and red, respectively (Figures 9a–9c). The line plots of the logarithmic values of the same four quantities along the subsolar line for the equatorial plane (Figure 9d) and against the Y axis at $Z = 0$ for the two X cuts (Figures 9e and 9f). The gradient of the logarithmic values of the four quantities along the subsolar line for the equatorial plane (Figure 9g) and against the Y axis at $Z = 0$ for the two X cuts (Figures 9h and 9i). The dash vertical lines in Figures 9g–9i mark the unity locations for two quantities with the innermost and outermost positions, color coded the same as the solid lines.

density ratio gradients are positive, primarily because the heavy ion density decreases with altitude. However, the ion mass and number density unities are clearly offset from the beta unity by $\sim 0.05 R_M$ (Figure 9d). To further examine this region, Figure 10 depicts the heavy ion mass density (black), H^+ density (blue), and the ratio of the two (red) along the Mars-Sun line (MSO X axis). Moving inward from the bow shock toward the planet, the heavy ion mass density increases with decreasing altitude, slowly at first, and then more rapidly as the mass density unity is approached. Interior to the unity, the heavy ion mass density rises steeply and soon dominates the total mass density. Meanwhile, the proton density remains nearly constant until the unity is reached and then drops gradually by a factor of ~ 3 . The inflection in the heavy ion mass density from 1.2 to $1.35 R_M$ corresponds to the dips of the ion density ratio gradients (Figure 9g), which are nearly colocated with strong beta gradients. This feature could be explained by an increase in ion production due to the electron impact ionization and charge exchange near the MPB [e.g., Crider *et al.*, 2000; Jin *et al.*, 2006] as well as the compression of planetary plasma by the solar wind. If we take the ion composition boundary to be centered on the mass density unity, then its thickness, as defined by the heavy ion mass density inflection, would be $\sim 0.1 R_M$.

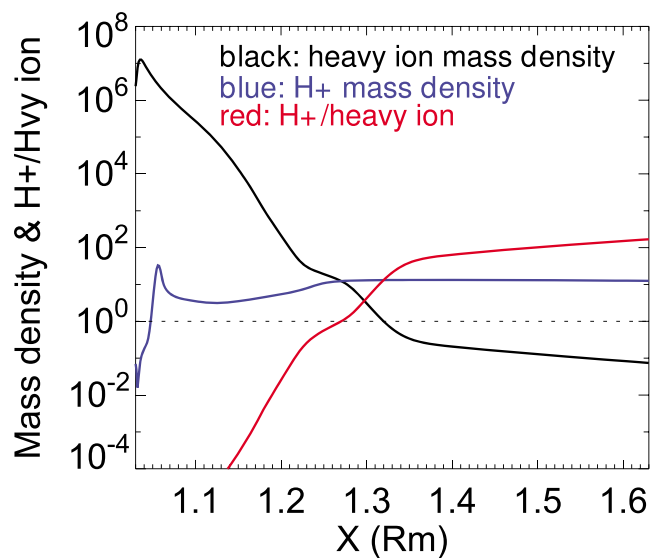


Figure 10. Heavy ion mass density (black), H^+ density (blue), and the ratio of H^+ density and heavy ions (red) against X axis. The unit for mass density is amu cm^{-3} , where amu is the atomic mass unit.

6. Discussion and Conclusions

This study quantitatively examined pressure and composition transitions in the Mars-solar wind interaction region by calculating gradients and unities of plasma β and β^* , as well as ion mass and number density ratios. We found that the unity contours are nearly colocated with the gradient extrema, so that they may be conveniently used to define physical boundaries in the system. Historically, these pressure and composition transitions have mostly been simplified as sharp, cylindrically symmetric boundaries. In this study, the unity contours and gradients of betas and ion density ratios have shown that these boundaries are structured and have a finite thickness, ranging from $0.05\text{--}0.1 R_M$ near the subsolar region to $1\text{--}1.5 R_M$ in the tail. The unity contours enclose magnetic lobes filled with planetary heavy ions to more than $10 R_M$ down tail. The pressure and composition gradients get progressively weaker and broader with increasing distance down the tail, presumably becoming indiscernible at large distances downstream. With a comprehensive set of instruments to measure the near Martian space environment, MAVEN data are being used to study these boundaries in detail [e.g., Matsunaga *et al.*, 2015]. The boundary shape and structure presented here can provide physical insight for these observational studies.

We examined the relationship between pressure and composition boundaries (corresponding to the observationally based MPB and ICB, respectively) by comparing unities and gradients of two betas and two ion density ratios. The unities are nearly colocated (Figure 9), it is easy to see that the unities mostly match with each other, except for the ion number density ratio unity, which is systematically interior to other unity boundaries. In the tail, the locations of the pressure and composition boundaries are very similar, which means the planetary heavy ions dominate not only the central plasma sheet but also the magnetic lobes. Even though heavy ions are more concentrated near the plasma sheet, the magnetic lobes are devoid of H^+ so that heavy ions still prevail. This means that ion escape down the tail occurs in both the plasma sheet and across the much larger cross-sectional area of the magnetic lobes. Downstream of the bow shock, Figure 10 shows that the decrease of solar wind proton density does not begin until the mass density ratio reaches unity. In addition, the model suggests that the ion composition boundary is structured, as revealed by an inflection in the heavy ion mass density gradient, which may be associated with enhanced electron impact ionization and charge exchange in this region.

While observationally, the MPB and ICB seem to occur close to one another, especially for $X > 0$, it has been unclear how these two boundaries are associated physically. In the tail region, the MF-MHD simulation exhibits a sharp outer edge to the lobes at the same location in both composition and beta. Magnetic field lines in the lobes are draped closely by Mars' upper atmosphere and may in some cases be connected to planetary crustal fields. The ionosphere could then plausibly provide the source of planetary ions in the lobes. The composition

and pressure boundaries deviate from one another in the tail near the $Y = 0$ plane for several reasons. First, there is a dense plasma sheet of planetary ions that dominates the pressure between the lobes. Second, there is an energetic plume of planetary ions in the $+Z$ direction that have very large gyroradii and move differently than the magnetic field. Third, the convection electric field accelerates planetary ions in the $-Z$ hemisphere back into the central tail region, which creates a small outward extension of the composition boundary in that direction (seen in Figures 9b and 9c).

The comparison between the boundaries determined from a MF-MHD simulation with the analytical fittings of MPB from Vignes *et al.* [2000] (based on MGS observations only) and Trotignon *et al.* [2006] (the combination of Phobos-2 and MGS observations) is shown in Figures 4a, 4d, 8a, and 8d. The two fits are highlighted in green solid line and red dashed line, respectively. In the tail, it is easy to see that the unity boundaries, except for the ion number density ratio presented in this study, match with the Vignes fitting and show little flaring, in contrast to a large flaring angle from the Trotignon fitting. The unity contour of the ion number density ratio, in fact, moves inward (toward the X axis) with distance down the tail, so the shape of this boundary depends on how it is defined. On the dayside, unity boundaries in this study are mostly located outside both fits, especially at higher solar zenith angle, and also exhibit a dawn-dusk asymmetry, probably due to the different in shock geometries (quasi-parallel versus quasi-perpendicular) at the dawnside and duskside. Existing data show a large spread of MPB locations at the tail [Vignes *et al.*, 2000], which can be attributed to many factors, such as the different upstream conditions and different locations of strong crustal magnetic fields with respect to the subsolar point. However, it might also be partially due to the structure and asymmetry of this boundary, which have so far not been considered in observational studies.

Finally, this study focuses on the three-dimensional shape and structure of the pressure and composition boundaries, which can be used as theoretical guidance for observational analyses. In particular, MAVEN data are now being used to study these boundaries in details [e.g., Matsunaga *et al.*, 2015]. Future work with a suite of MF-MHD models will investigate how the upstream conditions, strong crustal field locations, neutral atmosphere, and ionosphere affect these boundaries.

Acknowledgments

The authors would like to thank NASA for support of this project under grants NNX13AG26G and NNS14AH19G. The authors also thank support from the NASA Mars Scout Program. The authors thank Zhenguang Huang and Judit Szenté for teaching S. Xu Tecplot, which makes this study possible. The BATS-R-US code is publicly available from <http://csem.engin.umich.edu/tools/swmf>. For distribution of the model results used in this study, please contact C. Dong (dcfy@pppl.gov).

References

- Acuna, M., *et al.* (1999), Global distribution of crustal magnetization discovered by the Mars global surveyor mag/er experiment, *Science*, *284*(5415), 790–793.
- Arkani-Hamed, J. (2001), A 50-degree spherical harmonic model of the magnetic field of Mars, *J. Geophys. Res.*, *106*(E10), 23,197–23,208.
- Bertucci, C., C. Mazelle, M. Acuna, C. Russell, and J. Slavin (2005), Structure of the magnetic pileup boundary at Mars and Venus, *J. Geophys. Res.*, *110*, A01209, doi:10.1029/2004JA010592.
- Bertucci, C., F. Duru, N. Edberg, M. Fraenz, C. Martinecz, K. Szego, and O. Vaisberg (2012), The induced magnetospheres of Mars, Venus, and Titan, in *The Plasma Environment of Venus, Mars, and Titan*, edited by K. Szego, pp. 113–171, Springer, New York.
- Bößwetter, A., T. Bagdonat, U. Motschmann, and K. Sauer (2004), Plasma boundaries at Mars: A 3-D simulation study, *Ann. Geophys.*, *22*(12), 4363–4379, doi:10.5194/angeo-22-4363-2004.
- Bougher, S., D. Pawlowski, J. Bell, S. Nelli, T. McDunn, J. Murphy, M. Chizek, and A. Ridley (2015), Mars global ionosphere-thermosphere model: Solar cycle, seasonal, and diurnal variations of the Mars upper atmosphere, *J. Geophys. Res. Planets*, *120*, 311–342, doi:10.1002/2014JE004715.
- Brain, D., F. Bagenal, M. Acuña, and J. Connerney (2003), Martian magnetic morphology: Contributions from the solar wind and crust, *J. Geophys. Res.*, *108*(A12), 1424, doi:10.1029/2002JA009482.
- Brain, D., R. Lillis, D. Mitchell, J. Halekas, and R. Lin (2007), Electron pitch angle distributions as indicators of magnetic field topology near Mars, *J. Geophys. Res.*, *112*, A09201, doi:10.1029/2007JA012435.
- Brain, D., *et al.* (2010), A comparison of global models for the solar wind interaction with Mars, *Icarus*, *206*, 139–151, doi:10.1016/j.icarus.2009.06.030.
- Brecht, S. H. (1990), Magnetic asymmetries of unmagnetized planets, *Geophys. Res. Lett.*, *17*, 1243–1246, doi:10.1029/GL017i009p01243.
- Brecht, S. H. (1997), Hybrid simulations of the magnetic topology of Mars, *J. Geophys. Res.*, *102*, 4743–4750, doi:10.1029/96JA03205.
- Connerney, J., J. Espley, R. Oliverson, D. Sheppard, and G. Dibraccio (2015), First results from the MAVEN magnetic field investigation, paper presented at 46th Lunar and Planetary Science Conference, p. 1080, The Woodlands, Tex., 16–20 Mar.
- Cravens, T., J. Kozyra, A. Nagy, T. Gombosi, and M. Kurtz (1987), Electron impact ionization in the vicinity of comets, *J. Geophys. Res.*, *92*(A7), 7341–7353.
- Crider, D., *et al.* (2000), Evidence of electron impact ionization in the magnetic pileup boundary of Mars, *Geophys. Res. Lett.*, *27*(1), 45–48, doi:10.1029/1999GL003625.
- Crider, D. H., *et al.* (2002), Observations of the latitude dependence of the location of the Martian magnetic pileup boundary, *Geophys. Res. Lett.*, *29*(8), 1170, doi:10.1029/2001GL013860.
- Dong, C., S. W. Bougher, Y. Ma, G. Toth, A. F. Nagy, and D. Najib (2014), Solar wind interaction with Mars upper atmosphere: Results from the one-way coupling between the multifluid MHD model and the MTGCM model, *Geophys. Res. Lett.*, *41*, 2708–2715, doi:10.1002/2014GL059515.
- Dong, C., S. W. Bougher, Y. Ma, G. Toth, Y. Lee, A. F. Nagy, V. Tenishev, D. J. Pawlowski, M. R. Combi, and D. Najib (2015a), Solar wind interaction with the Martian upper atmosphere: Crustal field orientation, solar cycle, and seasonal variations, *J. Geophys. Res. Space Physics*, *120*, 7857–7872, doi:10.1002/2015JA020990.
- Dong, C., *et al.* (2015b), Multifluid MHD study of the solar wind interaction with Mars' upper atmosphere during the 2015 March 8th ICME event, *Geophys. Res. Lett.*, *42*, 9103–9112, doi:10.1002/2015GL065944.

- Dubinin, E., M. Fränz, J. Woch, E. Roussos, S. Barabash, R. Lundin, J. Winningham, R. Frahm, and M. Acuña (2006), Plasma morphology at Mars. Aspera-3 observations, *Space Sci. Rev.*, *126*(1–4), 209–238.
- Dubinin, E., et al. (2008), Structure and dynamics of the solar wind/ionosphere interface on Mars: MEX-ASPERA-3 and MEX-MARSIS observations, *Geophys. Res. Lett.*, *35*, L11103, doi:10.1029/2008GL033730.
- Fang, X., Y. Ma, D. Brain, Y. Dong, and R. Lillis (2015), Control of Mars global atmospheric loss by the continuous rotation of the crustal magnetic field: A time-dependent MHD study, *J. Geophys. Res. Space Physics*, *120*, 10,926–10,944, doi:10.1002/2015JA021605.
- Fränz, M., E. Dubinin, E. Roussos, J. Woch, J. Winningham, R. Frahm, A. Coates, A. Fedorov, S. Barabash, and R. Lundin (2006), Plasma moments in the environment of Mars, *Space Sci. Rev.*, *126*(1–4), 165–207.
- Glocer, A., G. Tóth, Y. Ma, T. Gombosi, J.-C. Zhang, and L. M. Kistler (2009), Multifluid Block-Adaptive-Tree Solar wind Roe-type Upwind Scheme: Magnetospheric composition and dynamics during geomagnetic storms—Initial results, *J. Geophys. Res.*, *114*, A12203, doi:10.1029/2009JA014418.
- Halekas, J., et al. (2015), Time-dispersed ion signatures observed in the Martian magnetosphere by MAVEN, *Geophys. Res. Lett.*, *42*, 8910–8916, doi:10.1002/2015GL064781.
- Harnett, E. M., and R. M. Winglee (2005), Three-dimensional fluid simulations of plasma asymmetries in the Martian magnetotail caused by the magnetic anomalies, *J. Geophys. Res.*, *110*, A07226, doi:10.1029/2003JA010315.
- Jakosky, B. M., et al. (2015a), The Mars atmosphere and volatile evolution (MAVEN) mission, *Space Sci. Rev.*, *195*, 3–48.
- Jakosky, B. M., et al. (2015b), MAVEN observations of the response of Mars to an interplanetary coronal mass ejection, *Science*, *350*(6261), aad0210.
- Jin, H., K. Maezawa, and T. Mukai (2006), Effects of charge exchange and electron impact ionization on the formation of the magnetic pileup boundary at Mars, *J. Geophys. Res.*, *111*, A05306, doi:10.1029/2005JA011127.
- Kallio, E., et al. (2006), Ion escape at Mars: Comparison of a 3-D hybrid simulation with Mars Express IMA/ASPERA-3 measurements, *Icarus*, *182*, 350–359, doi:10.1016/j.icarus.2005.09.018.
- Lee, Y., M. R. Combi, V. Tenishev, and S. W. Bougher (2014a), Hot carbon corona in Mars' upper thermosphere and exosphere: 1. Mechanisms and structure of the hot corona for low solar activity at equinox, *J. Geophys. Res. Planets*, *119*, 905–924, doi:10.1002/2013JE004552.
- Lee, Y., M. R. Combi, V. Tenishev, and S. W. Bougher (2014b), Hot carbon corona in Mars' upper thermosphere and exosphere: 2. Solar cycle and seasonal variability, *J. Geophys. Res. Planets*, *119*, 2487–2509, doi:10.1002/2014JE004669.
- Lee, Y., M. R. Combi, V. Tenishev, S. W. Bougher, and R. J. Lillis (2015), Hot oxygen corona at Mars and the photochemical escape of oxygen: Improved description of the thermosphere, ionosphere, and exosphere, *J. Geophys. Res. Planets*, *120*, 1880–1892, doi:10.1002/2015JE004890.
- Liemohn, M. W., Y. Ma, R. A. Frahm, X. Fang, J. U. Kozyra, A. F. Nagy, J. D. Winningham, J. R. Sharber, S. Barabash, and R. Lundin (2006), Mars global MHD predictions of magnetic connectivity between the dayside ionosphere and the magnetospheric flanks, *Space Sci. Rev.*, *126*, 63–76, doi:10.1007/s11214-006-9116-8.
- Liemohn, M. W., Y. Ma, A. Nagy, J. Kozyra, J. Winningham, R. Frahm, J. Sharber, S. Barabash, and R. Lundin (2007), Numerical modeling of the magnetic topology near Mars auroral observations, *Geophys. Res. Lett.*, *34*, L24202, doi:10.1029/2007GL031806.
- Ma, Y., A. F. Nagy, K. C. Hansen, D. L. DeZeeuw, T. I. Gombosi, and K. Powell (2002), Three-dimensional multispecies MHD studies of the solar wind interaction with Mars in the presence of crustal fields, *J. Geophys. Res.*, *107*(A10), 1282, doi:10.1029/2002JA009293.
- Ma, Y., A. F. Nagy, I. V. Sokolov, and K. C. Hansen (2004), Three-dimensional, multispecies, high spatial resolution MHD studies of the solar wind interaction with Mars, *J. Geophys. Res.*, *109*, A07211, doi:10.1029/2003JA010367.
- Ma, Y., X. Fang, C. T. Russell, A. F. Nagy, G. Toth, J. G. Luhmann, D. A. Brain, and C. Dong (2014), Effects of crustal field rotation on the solar wind plasma interaction with Mars, *Geophys. Res. Lett.*, *41*, 6563–6569, doi:10.1002/2014GL060785.
- Ma, Y., et al. (2015), MHD model results of solar wind interaction with Mars and comparison with MAVEN plasma observations, *Geophys. Res. Lett.*, *42*, 9113–9120, doi:10.1002/2015GL065218.
- Matsunaga, K., et al. (2015), Comparison of Martian magnetic pileup boundary with ion composition boundary observed by MAVEN, Abstract P21A-2071 presented at 2015 Fall Meeting, AGU, San Francisco, Calif., 14–18 Dec.
- Modolo, R., G. M. Chanteur, E. Dubinin, and A. P. Matthews (2006), Simulated solar wind plasma interaction with the Martian exosphere: Influence of the solar EUV flux on the bow shock and the magnetic pile-up boundary, *Ann. Geophys.*, *24*, 3403–3410, doi:10.5194/angeo-24-3403-2006.
- Moore, T., and D. Delcourt (1995), The geopause, *Rev. Geophys.*, *33*(2), 175–209.
- Nagy, A., et al. (2004), The plasma environment of Mars, in *Mars' Magnetism and Its Interaction With the Solar Wind*, edited by D. Winterhalter, M. Acuña, and A. Zakharov, pp. 33–114, Springer, Netherlands.
- Najib, D., A. F. Nagy, G. Tóth, and Y. Ma (2011), Three-dimensional, multifluid, high spatial resolution MHD model studies of the solar wind interaction with Mars, *J. Geophys. Res.*, *116*, A05204, doi:10.1029/2010JA016272.
- Powell, K. G., P. L. Roe, T. J. Linde, T. I. Gombosi, and D. L. De Zeeuw (1999), A solution-adaptive upwind scheme for ideal magnetohydrodynamics, *J. Comput. Phys.*, *154*, 284–309, doi:10.1006/jcph.1999.6299.
- Riedler, W., et al. (1989), Magnetic fields near Mars: First results, *Nature*, *341*(6243), 604–607.
- Sauer, K., T. Roatsch, U. Motschmann, K. Schwingenschuh, R. Lundin, H. Rosenbauer, and S. Livi (1992), Observations of plasma boundaries and phenomena around Mars with Phobos 2, *J. Geophys. Res.*, *97*(A5), 6227–6233.
- Sauer, K., A. Bogdanov, and K. Baumgärtel (1994), Evidence of an ion composition boundary (protonopause) in bi-ion fluid simulations of solar wind mass loading, *Geophys. Res. Lett.*, *21*(20), 2255–2258.
- Schunk, R., and A. Nagy (2009), *Ionospheres*, Cambridge Univ. Press, Cambridge, U. K.
- Simon, S., A. Boesswetter, T. Bagdonat, and U. Motschmann (2007), Physics of the ion composition boundary: A comparative 3-D hybrid simulation study of Mars and Titan, *Ann. Geophys.*, *25*(1), 99–115, doi:10.5194/angeo-25-99-2007.
- Tóth, G., et al. (2012), Adaptive numerical algorithms in space weather modeling, *J. Comput. Phys.*, *231*, 870–903, doi:10.1016/j.jcp.2011.02.006.
- Trotignon, J., C. Mazelle, C. Bertucci, and M. Acuña (2006), Martian shock and magnetic pile-up boundary positions and shapes determined from the Phobos 2 and Mars Global Surveyor data sets, *Planet. Space Sci.*, *54*(4), 357–369, doi:10.1016/j.pss.2006.01.003.
- Trotignon, J. G., E. Dubinin, R. Grard, S. Barabash, and R. Lundin (1996), Martian planetopause as seen by the plasma wave system onboard Phobos 2, *J. Geophys. Res.*, *101*(A11), 24,965–24,977.
- Vignes, D., C. Mazelle, H. Rme, M. H. Acuña, J. E. P. Connerney, R. P. Lin, D. L. Mitchell, P. Cloutier, D. H. Crider, and N. F. Ness (2000), The solar wind interaction with Mars: Locations and shapes of the bow shock and the magnetic pile-up boundary from the observations of the MAG/ER experiment onboard Mars Global Surveyor, *Geophys. Res. Lett.*, *27*, 49–52, doi:10.1029/1999GL010703.
- Xu, S., M. W. Liemohn, and D. L. Mitchell (2014), Solar wind electron precipitation into the dayside Martian upper atmosphere through the cusps of strong crustal fields, *J. Geophys. Res. Space Physics*, *119*, 10,100–10,115, doi:10.1002/2014JA020363.